



# Synthesis and analysing the structural, optical, morphological, photocatalytic and magnetic properties of TiO<sub>2</sub> and doped (Ni and Cu) TiO<sub>2</sub> nanoparticles by sol–gel technique

T. Raguram<sup>1</sup> · K. S. Rajni<sup>1</sup>

Received: 15 December 2018 / Accepted: 23 March 2019 / Published online: 2 April 2019  
© Springer-Verlag GmbH Germany, part of Springer Nature 2019

## Abstract

In the present work, Ni<sup>2+</sup> and Cu<sup>2+</sup> ions are doped with TiO<sub>2</sub> using sol–gel technique. The effects of Ni and Cu doping in TiO<sub>2</sub> matrix are characterized by XRD, Micro-Raman, FTIR, UV–DRS, PL, and FESEM with EDS. Furthermore, it is analyzed for photocatalytic activity and magnetic applications. From XRD analysis, it is observed that the peaks corresponding to the planes match with the JCPDS data [anatase: 89-4203] of TiO<sub>2</sub>. The crystallite size of the doped samples is found to be greater than that of TiO<sub>2</sub>. Micro-Raman analysis shows the confirmation of anatase phase of TiO<sub>2</sub>. FTIR analysis confirms the presence of functional groups which are presented in the prepared samples. From UV–DRS, the band-gap values of TiO<sub>2</sub> and doped TiO<sub>2</sub> (Ni<sup>2+</sup>, Cu<sup>2+</sup>) are found to be 3.25, 2.48, and 1.25 eV. Photoluminescence (PL) results show an emission edge of Ni- and Cu-doped TiO<sub>2</sub> is red shifted which is due to the vacancies of titanium and oxygen imported subsequently during doping. The surface morphology and the elemental composition of Ni- and Cu-doped TiO<sub>2</sub> nanoparticles are also analyzed. The photocatalytic activity of all the prepared samples are assessed by methylene blue dye as testing pollutant and visible radiation. The test reveals that Cu–TiO<sub>2</sub>, Ni–TiO<sub>2</sub>, and TiO<sub>2</sub> show the degradation efficiency of 68.14, 61.04, and 33.32%, thereby showing that the doped TiO<sub>2</sub> are more efficient in degrading the pollutant and can be applied for future photocatalytic applications. From VSM analysis, the saturation magnetization of Ni–TiO<sub>2</sub> and Cu–TiO<sub>2</sub> is found to be weak and can be improved by the synthesis process and the proportion of dopant.

## 1 Introduction

To manipulate the properties and, hence, to obtain the desired functionality of solids, dopants act an important character, particularly in a field of microelectronics and optoelectronics. Recently, the search for materials which is both the properties of semiconductors and ferromagnetism (FM) has derived into the valuable field of material sciences to achievement of the spin degrees of freedom for the carrier. Thus, important research is in progress on investigating the promising of spin functionality of induced ferromagnetism in the non-magnetic semiconductors adding dopants of magnetic ions via dilute concentrations and thereby obtaining diluted magnetic semiconductors (DMS) [1, 2]. DMS exhibit both the semiconducting and the magnetic properties such

as ferromagnetism and magnetoelectricity. In DMS, the interaction (exchange) between the electrons and affects the change in magnetic properties, which, in turn, leads to shift in the bandgap [3]. Studies on DMS have been intensified recently due to their promising applications in spintronics [4]. DMS materials might be components of new technologies such as non-volatile memories, high-speed devices for data handling and reduced power expenditure, and conceivably tiny structures [5–8]. However, many experimental reports show maintain lower temperature, low moment of magnetic ordering [9, 10]. In support of many possible results reported in the literature, DMS has still challenged by the incorporation of dopants which are consistency, possibilities of secondary ferromagnetic phases, and contamination issues [11]. The most intensively explored field of DMS research is the doping of regular III–V or II–VI semiconductors, where the underlying lattice has wurtzite or zinc-blende structure with transition metal ions such as Cr, Mn, Fe, Co, and Ni [12]. In general, the magnetic (3d) ions in DMS materials are located on substitutional and/or interstitial sites of the semiconducting host [13]. DMSs

✉ K. S. Rajni  
ks\_rajani@cb.amrita.edu

<sup>1</sup> Department of Sciences, Amrita School of Engineering,  
Amrita Vishwa Vidyapeetham, Coimbatore, India

based on II–IV metal oxide wide band-gap semiconductors such as ZnO, TiO<sub>2</sub>, and SnO have attracted considerable attention for their promising high-temperature ferromagnetization [14]. Hence, the dependence of magnetic ion dopant effects in oxides have inspiring possibilities and new physics (different spin functionality). Most extensive research in this field has been done on two wide band-gap functional metal oxides, namely TiO<sub>2</sub> and ZnO [15].

Recently, various nanostructures of metal oxides have been introduced for breaking through the barriers. On account of the high specific surface area and its structures, they prefer good performance [16]. TiO<sub>2</sub> is a wide band-gap *n*-type semiconductor with bandgap 3.1 eV at room temperature which is an essential element of devices like photocatalytic reactors, photoelectrochemical cells, etc. [17, 18]. Titanium oxide (TiO<sub>2</sub>) is a bandgap of 3.2 eV, nontoxic, low-cost, physical and chemical stability, and unique electronic and optical properties [19, 20]. The major drawback is absorption in the ultraviolet regime and fast electron–hole pair recombination.

These drawbacks are overcome by doping of metals such as Ni<sup>2+</sup> and Cu<sup>2+</sup>. The doping of Ni<sup>2+</sup> and Cu<sup>2+</sup> results in the suppression of electron–hole pair recombination on the surface of the photocatalyst. In certain semiconductor, low valence dopant improves the photocatalytic activity of the material.

TiO<sub>2</sub> exhibits the characteristics of both the semiconducting and the magnetic materials; it can realize the dual control of both electric and magnetic fields by using the electric charge and spin properties of electrons. To achieve the application of the DMS TiO<sub>2</sub>, it is important to prepare room-temperature DMS materials with high saturation magnetization intensity. The room-temperature ferromagnetism of DMS can be improved by changing the synthesis method, annealing atmosphere, and doping of different metallic or

nonmetallic ions in the host lattices [21]. Therefore, desired doping of these wide band-gap nanostructures can provide important materials for the application of magnetic processes [22]. The different magnetic ions are doped into TiO<sub>2</sub> for attaining the room-temperature ferromagnetism (RTFM) which is one of the appealing conditions in spintronics research. The synthesis of materials for DMS includes molecular beam epitaxy (MBE) [23, 24], pulsed laser deposition [25], ion implantation [26], and sol–gel technique [27]. In the present work, TiO<sub>2</sub> and Ni<sup>2+</sup>, and Cu<sup>2+</sup> doped with TiO<sub>2</sub> nanoparticles are prepared by sol–gel technique. This technique gives the advantages such as stoichiometry ratio, high crystallinity, and purity [28–30]. The physical characteristics of the prepared nanoparticles are analyzed, and the photocatalytic performance of as-prepared Ni- and Cu-doped TiO<sub>2</sub> is evaluated by MB degradation. Figure 1 shows the schematic diagram of Cu–TiO<sub>2</sub>. In addition, Ni- and Cu-doped TiO<sub>2</sub> are analyzed for diluted magnetic semi-conducting properties.

## 2 Experimental

### 2.1 Synthesis of TiO<sub>2</sub>, Ni-, and Cu-doped TiO<sub>2</sub> nanoparticles

The TiO<sub>2</sub> nanoparticles are prepared by adding 2.5 ml of deionized water mixed with 10 ml of isopropanol and stirred for half an hour, and 0.5 M titanium tetraisopropoxide (Sigma-Aldrich) is added drop by drop into the mixed solution. After an hour, 1 ml of conc. HNO<sub>3</sub> is added into the solution and the solution (mixture) vigorously stirred for 45 min. The obtained gel is dried at 80 °C for 5 h and then annealed at 300 °C for 3 h. The Ni<sup>2+</sup>- and Cu<sup>2+</sup>-doped TiO<sub>2</sub> is prepared by adding liquid solution of nickel nitrate

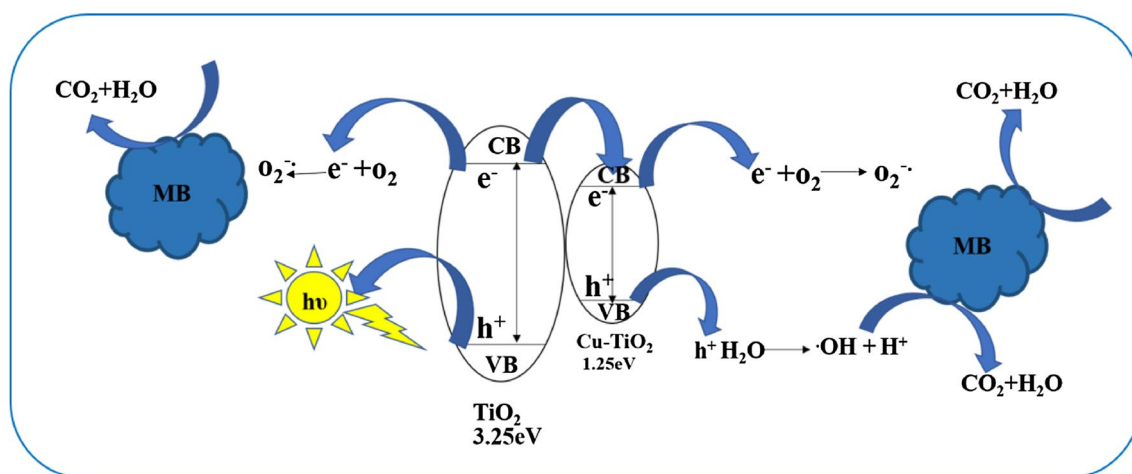


Fig. 1 Schematic diagram of photocatalytic performance of Cu–TiO<sub>2</sub> nanoparticles

hexahydrate (NICE) and copper nitrate trihydrate (NICE) of desired concentration (0.3 M) drop by drop to the mixture accompanied by continuous stirring. The process is repeated to get the desired Ni- and Cu-doped TiO<sub>2</sub> nanoparticles.

## 2.2 Photocatalytic performance evaluation

For photocatalyst powder, 0.05 g of photocatalysts is dispersed into 50 mL of  $1 \times 10^{-5}$  M aqueous solution of dyes and irradiated under simulated 150 W tungsten lamp (with main wavelength at 465 nm) under continuous stirring. Samples from the aliquots from the solutions are collected at time intervals of 10 min, and analyzed to evaluate the concentration of MB by a Shimadzu UV-1600 spectrophotometer ( $\lambda = 664$  nm). The photocatalytic degradation efficiency is calculated according to the following equation [31]:

$$\%D = \left( \frac{C_0 - C_t}{C_0} \right) \times 100,$$

where  $C_0$  is the initial concentration,  $C_t$  is the equilibrium concentration at time 't', and  $D$  is the degradation rate (%).

## 2.3 Characterisation

The structural analysis of the prepared samples are carried out using X-ray diffractometer (RIGAKU ULTIMA IV) with CuK $\alpha$  radiation wavelength of 1.541 Å. The optical diffuse reflectance spectra (DRS) are recorded in the wavelength range of 200–2500 nm by UV–DRS spectrophotometer (UV 2600 ISR). Using Micro-Raman (Renishaw in Via Raman Microscope) analysis to confirm the structure and corresponding modes of vibrations, functional groups are analyzed by FTIR using Perkin Elmer spectrophotometer in the range of 4000–400 cm<sup>-1</sup>. The surface morphology and elemental analysis of the prepared samples are examined by Field-Emission Scanning Electron microscopy (ZEISS). The photoluminescence (PL) spectra are performed by RF 6000 fluorescence spectrophotometer. The magnetic properties of the Ni- and Cu-doped TiO<sub>2</sub> nanoparticles are investigated by a vibrating sample magnetometer (Lakeshore V650).

## 3 Results and discussion

### 3.1 Structural analysis

Figure 2 shows the PXRD patterns of synthesized TiO<sub>2</sub>, Ni-, and Cu-doped TiO<sub>2</sub> nanoparticles prepared by sol–gel technique. From Fig. 2, it is noted that the synthesized TiO<sub>2</sub> shows the pure anatase phase with tetragonal structure and the planes (101), (112), (200), (105), (211), (204), (116), (220), and (215) matches, with the JCPDS data

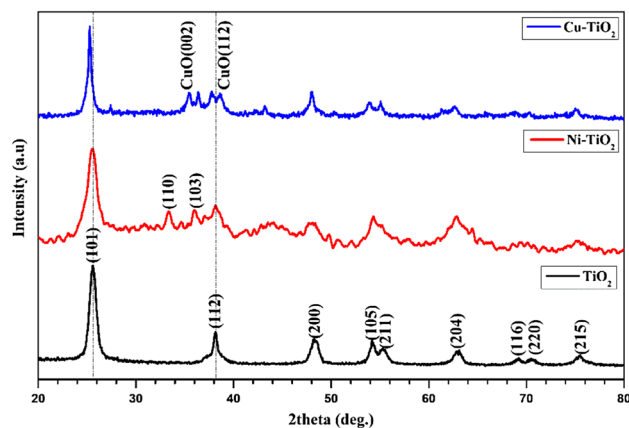


Fig. 2 PXRD pattern of TiO<sub>2</sub>, Ni-, and Cu-doped TiO<sub>2</sub> nanoparticles

(Card no. 89-4203). In nickel-doped TiO<sub>2</sub>, additional two planes (110) and (103) correspond to anatase phase of TiO<sub>2</sub> which are also observed. Due to the surface adsorption of Ni<sup>2+</sup> on TiO<sub>6</sub> via hydrogen bonding and its changes their fable structure and to permit restraint the hydrolysis and polycondensation reactions which retarded the phase transformation, no other peaks of nickel oxide in the Ni-doped TiO<sub>2</sub> which is attributed to the low concentration or elegant diffusion of Ni<sup>2+</sup> on TiO<sub>2</sub> matrix [32, 33]. In Cu-doped TiO<sub>2</sub> nanoparticles, two additional planes (002) and (112) corresponding to CuO [PDF: 48-1548] with monoclinic lattice structure which is also observed. The results clearly indicate that addition of dopants did not affect the tetragonal phase of the host nanomaterial. In addition, the incorporation of dopants in host lattices results in the peak shift (101) towards the lower angle which is attributed to the ionic radii of Ni<sup>2+</sup> (0.69 Å) and Cu<sup>2+</sup> (0.73 Å) which are greater than Ti<sup>4+</sup> (0.61 Å). Using the Scherrer equation [34]:

$$D = \frac{k\lambda}{\beta \cos \theta}.$$

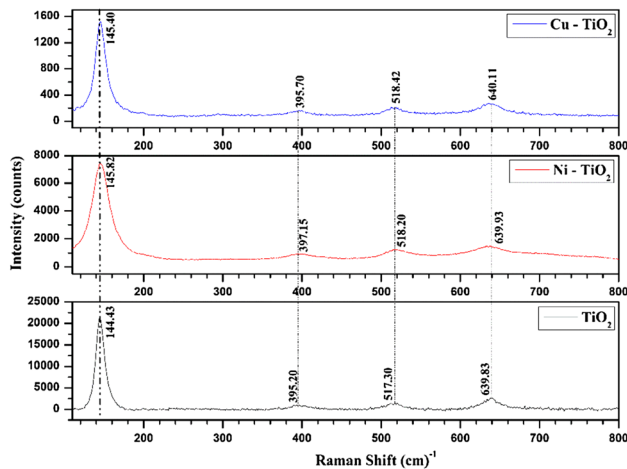
The crystallite size is calculated for the most intense (101) plane which is found to be 9 nm for TiO<sub>2</sub>, around 22 nm for Ni- and Cu-doped TiO<sub>2</sub>. The microstrain is calculated for the prepared samples using the formula:

$$\varepsilon = \frac{\beta \cos \theta}{4}.$$

From Table 1, it is noted that the microstructural strain of Ni<sup>2+</sup> and Cu<sup>2+</sup> ion-doped TiO<sub>2</sub> is found to be less than TiO<sub>2</sub>. The variation in the microstructural strain of doped samples results in reducing the lattice defects in the crystals. This is due to the Ni<sup>2+</sup> and Cu<sup>2+</sup> ions are strongly

**Table 1** Microstructural parameters of TiO<sub>2</sub>, Ni-, and Cu-doped TiO<sub>2</sub> nanoparticles

Samples	$2\theta$ (°)	Crystallite size (nm)	Lattice constant (Å)		Volume of unit cell (Å) <sup>3</sup>	Strain (10 <sup>-6</sup> )
			$a$ (3.785)	$c$ (9.514)		
TiO <sub>2</sub>	25.60	9.00	3.780	9.459	135.17	0.0965
Ni-TiO <sub>2</sub>	25.51	22.16	3.771	9.450	134.41	0.0369
Cu-TiO <sub>2</sub>	25.27	22.15	3.779	9.514	135.94	0.0366

**Fig. 3** Micro-Raman spectra of TiO<sub>2</sub>, Ni-, and Cu-doped TiO<sub>2</sub> nanoparticles

introduced into the host (Ti<sup>4+</sup>) crystal matrix in the substitutional mode which reflects reducing the lattice distortion. Higher concentration of Ni<sup>2+</sup> and Cu<sup>2+</sup> in TiO<sub>2</sub> helps the agglomeration of the small crystallites which in turn reduce the lattice defects in the prepared samples [35]. In general, increasing the size of the agglomerations that are formed will minimize the crystal defects, including the microstrain [35–37]. The lattice constants ( $a$  and  $c$ ) of synthesized nanoparticles are calculated using the formula:

$$\frac{1}{d^2} = \frac{(h^2 + k^2)}{a^2} + \frac{l^2}{c^2}.$$

The lattice constant of Ni- and Cu-doped TiO<sub>2</sub> is found to be less than that of TiO<sub>2</sub>. The variation in the lattice parameter is attributed to the differences in the valencies and ionic radii of Ni<sup>2+</sup> (0.69 Å), Cu<sup>2+</sup> (0.73 Å), and Ti<sup>4+</sup> (0.61 Å), respectively [37, 38].

### 3.2 Micro-Raman analysis

Micro-Raman spectra of TiO<sub>2</sub>, Ni-, and Cu-doped TiO<sub>2</sub> nanoparticles are shown in Fig. 3. Raman spectroscopy is used to investigate the structure and phase composition

of the prepared samples [39, 40]. In general, tetragonal anatase phase of TiO<sub>2</sub> shows six Raman active modes and three infrared active modes are  $A_{1g} + 2B_{1g} + 3E_g$  and  $A_{2u} + 2E_u$  [41].  $A_{1g}$  mode centered around 513 cm<sup>-1</sup>,  $2B_{1g}$  modes at 399 and 519 cm<sup>-1</sup>, and  $3E_g$  modes at 145, 197, and 369 cm<sup>-1</sup> [42]. From Fig. 3, it is noted that  $E_g$ ,  $B_{1g}$ , and  $A_{1g}$  are observed at 144.34, 394.47, 515.80, and 639.50 cm<sup>-1</sup> for TiO<sub>2</sub> nanoparticles. The studies shows that shift in the principle peak (144 cm<sup>-1</sup>) of Ni<sup>2+</sup>- and Cu<sup>2+</sup>-doped samples towards higher wavenumber compared to TiO<sub>2</sub> which is attributed to the result of vacancies in the oxygen surface induced by dopants [43–45]. In addition, the distortion of lattice structure of TiO<sub>2</sub> due to the dopants of ionic radii is greater than that of host material. To continue the neutrality, the dopants create oxygen vacancies in TiO<sub>2</sub> lattice which is also observed in the present study [46]. Due to the creation of O<sup>-</sup> vacancies, the lattices get contracted and the peaks are moved from lower to higher wave number region [47]. In the present work from the microstructural analysis, it is noted that the doped TiO<sub>2</sub> shows the contraction in the lattice parameters. In addition, some researchers reported the peak broadening and shifting due to the quantum size effect [48]. If the substitutions of Ni<sup>2+</sup> and Cu<sup>2+</sup> take place with Ti<sup>4+</sup>, Ti–O–Ti bond get perturbed and it reflects the Ni–O–Ti and Cu–O–Ti which are formed. The disturbance of Ti–O–Ti bonds that results in Ni–O bond further affects the Raman active modes and it starts the peak shifting and broadening [49]. Apart from the main peaks, the other peaks are observed at 241.43, 288.89, 345.35, 461.50, 611.99, and 704.41 cm<sup>-1</sup> which are due to the Ni–TiO<sub>3</sub> attributed to the concentration of Ni<sup>2+</sup>; similar type of observations are reported by Chuang et al. [50].

### 3.3 Functional group analysis

The recorded FTIR spectra of the prepared samples are shown in Fig. 4. It is noted that the broad peak around 3420 cm<sup>-1</sup> and 1620 cm<sup>-1</sup> is due to the stretching vibrations of NH<sub>3</sub><sup>+</sup> and COO<sup>-</sup>. The CH<sub>3</sub> deformation modes are assigned to 1381 cm<sup>-1</sup>. The spectra of lower wavenumber region of the band around 438 cm<sup>-1</sup> are due to the bending vibrations of M–O such as Ti–O and Ti–O–Ti frame work bonds [51]. From the spectra of TiO<sub>2</sub>, Ni-, and Cu-doped TiO<sub>2</sub>, it is noted that a slight shift in the bands/peaks position and the change in the intensity of bands are observed which

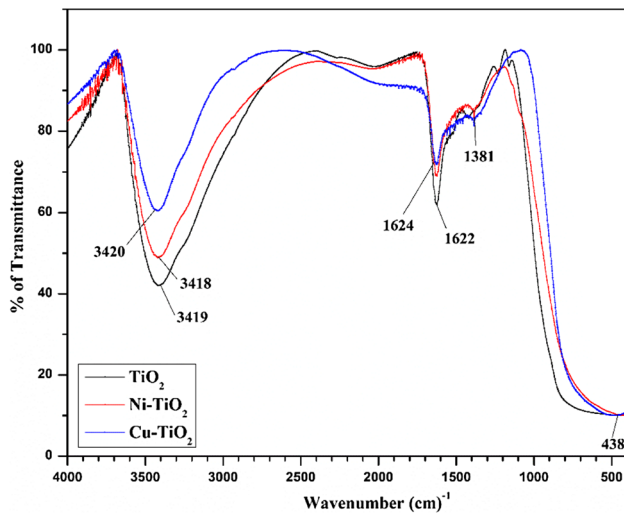


**Fig. 4** FTIR spectra of TiO<sub>2</sub>, Ni-, and Cu-doped TiO<sub>2</sub> nanoparticles

may be due to the presence of the dopants in the interstitials of the lattices of the doped samples [51, 52].

### 3.4 Optical analysis

The optical reflectance spectra of TiO<sub>2</sub>, Ni-, and Cu-doped TiO<sub>2</sub> nanoparticles are shown in Fig. 5. From the figure, it is noted that a sharp decrease in reflectance around 380 nm is observed for TiO<sub>2</sub> due to the electron transfers from O<sup>2-</sup> 2*p* states of valence band (VB) to Ti<sup>3+</sup> 3*d* states of conduction band (CB) [53] and the absorption edge is red shifted, when TiO<sub>2</sub> is doped with Ni and Cu [54, 55]. The conversion of reflectance spectra into Kubelka–Munk function [56]

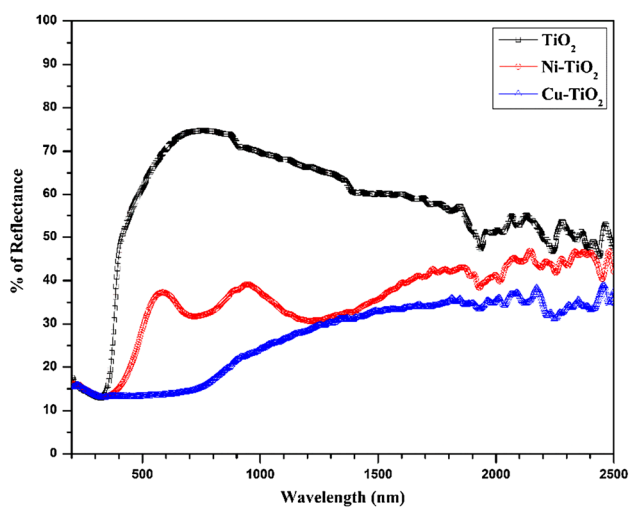


**Fig. 5** UV-DRS spectra of TiO<sub>2</sub>, Ni-, and Cu-doped TiO<sub>2</sub> nanoparticles

(equivalent to the absorption coefficient),  $F(R_\alpha)$ , is given by the relation:

$$F(R_\alpha) = \frac{(1 - R_\alpha)^2}{2R_\alpha},$$

where  $R_\alpha$  is the reflectance of a sample with respect to reference at each wavelength. From the Fig. 6, it is noted that both TiO<sub>2</sub>, Ni- and Cu-doped TiO<sub>2</sub> show direct allowed transitions and band-gap energy values are found to be 3.25, 2.48, and 1.25 eV. Due to the Ni<sup>2+</sup> and Cu<sup>2+</sup> doping, the transitions electrons are not straightly transfer to conduction band of TiO<sub>2</sub> because of *s-d* states of Ni<sup>2+</sup> and Cu<sup>2+</sup> and oxygen vacancies are captured the transitions electrons. The sub-band states of Ni<sup>2+</sup> and Cu<sup>2+</sup> and oxygen vacancies are the major role of decreasing band-gap values compared to TiO<sub>2</sub> [49]. The decreasing band-gap energy is inducing to photocatalytic degradation of organic MB dye.

### 3.5 Photocatalytic activity

The basic process for the photocatalysis of organic compounds by TiO<sub>2</sub> is the generation of electron–hole pair [57]. The generated electrons are attracted to the metal particle due to the difference in the work function of TiO<sub>2</sub> and metal particle. The photogenerated holes oxidized organic molecule (R<sup>+</sup>) or react with OH<sup>-</sup> or H<sub>2</sub>O, oxidizing them into radicals of OH, resulting in degradation of organic compounds adsorbed on to the TiO<sub>2</sub> surface. It is observed that, within the reaction period of 60 min, the photocatalyst has attained conversion. The photocatalytic degradation of MB using TiO<sub>2</sub> initially confers and remains steady with time which is due to higher bandgap of TiO<sub>2</sub>. However, the addition of Ni and Cu to TiO<sub>2</sub>

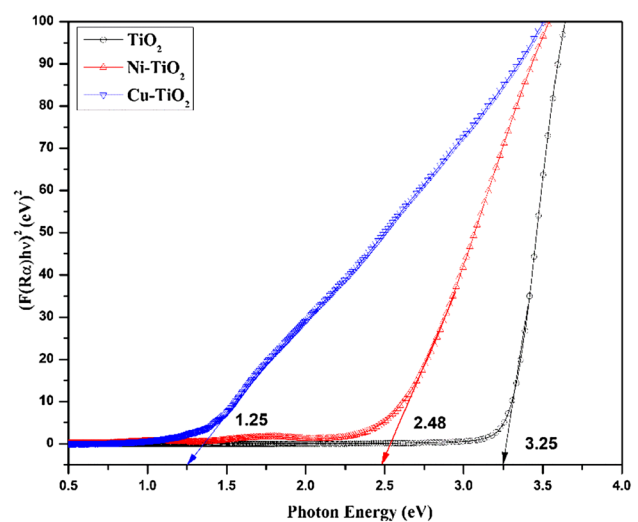


**Fig. 6** Kubelka–Munk plot of TiO<sub>2</sub>, Ni-, and Cu-doped TiO<sub>2</sub> nanoparticles



did not show the same photocatalytic behavior as TiO<sub>2</sub>. The steps in photocatalytic reduction of metals in TiO<sub>2</sub> are shown in the following [21, 22]:

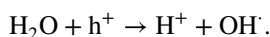
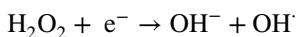
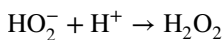
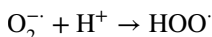
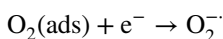
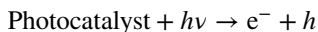


Figure 7a, b shows photocatalytic efficiency and degradation percentage (%) of as-synthesized photocatalysts in the degradation of MB ( $1 \times 10^{-5}$  M) solution under visible light irradiation. It is noted that the degradation of MB is faster for Cu-TiO<sub>2</sub> than Ni-TiO<sub>2</sub> which is attributed to the decreased bandgap of Cu-TiO<sub>2</sub> (1.25 eV) than Ni-TiO<sub>2</sub> (2.48 eV) as observed in DRS analysis.

The absorption of methylene blue decreases with increase in time which is due to the degradation of MB into carbon dioxide and water. Figure 8 shows temporal changes in

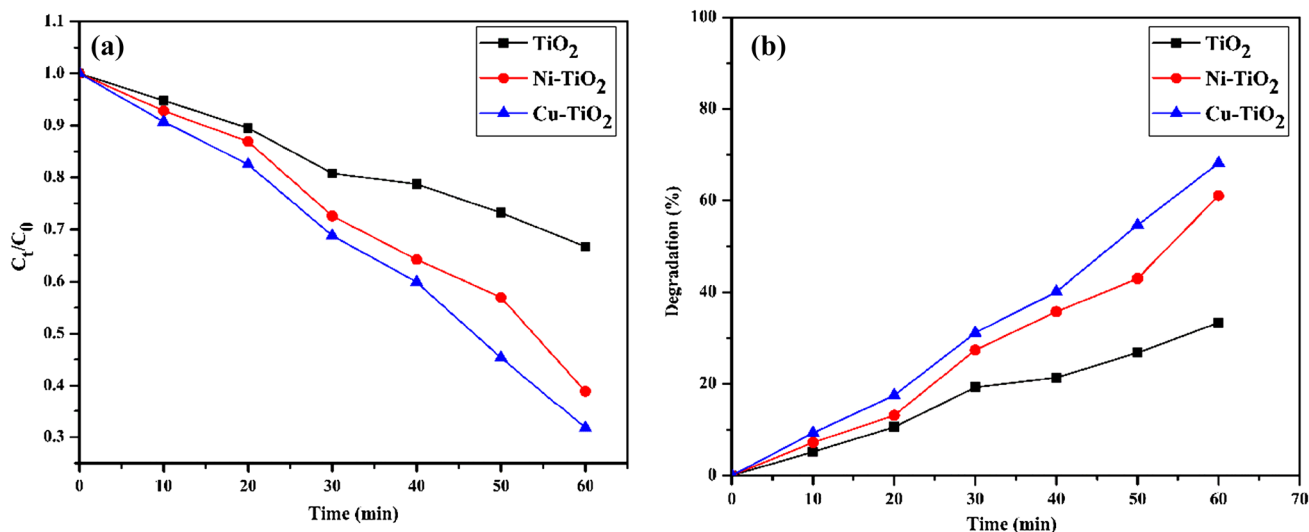


Fig. 7 a Photocatalytic efficiency and b degradation percentage (%) of as-synthesized photocatalysts in the degradation of MB ( $1 \times 10^{-5}$  M) solution under visible light irradiation

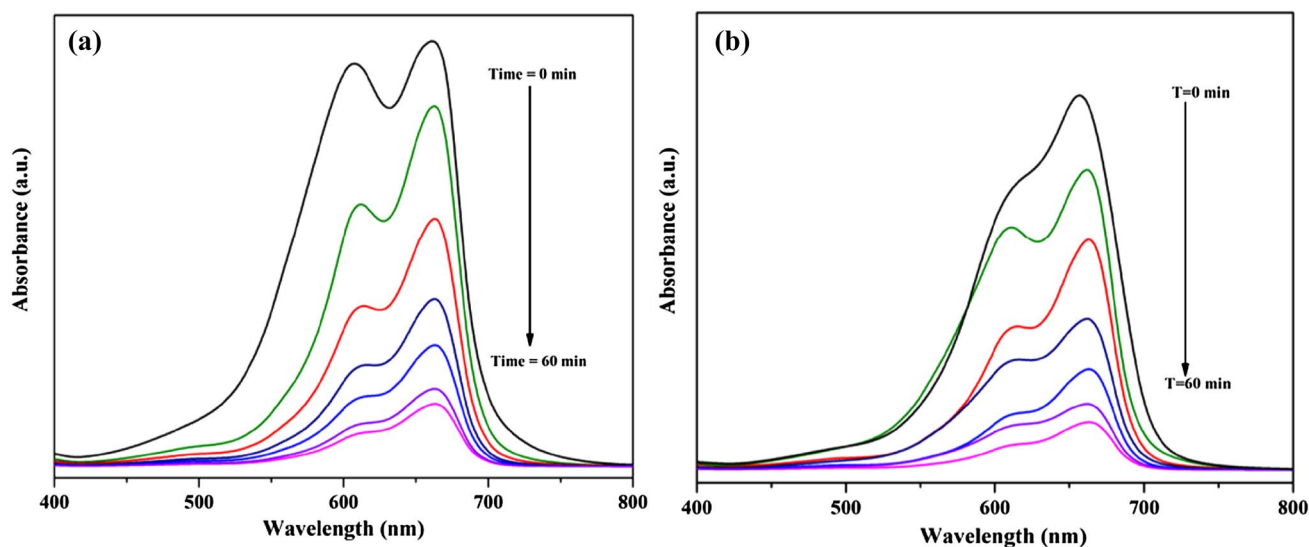
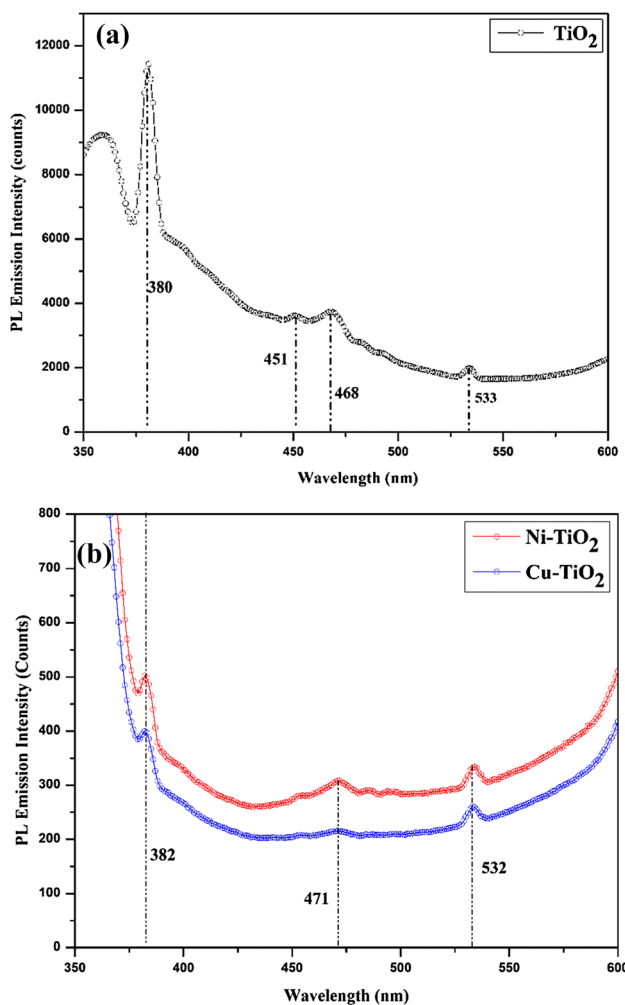


Fig. 8 Temporal changes in absorbance spectra of MB dye with time ( $1 \times 10^{-5}$  M) under visible light irradiation using a Ni-TiO<sub>2</sub> and b Cu-TiO<sub>2</sub>

absorbance spectra of MB dye with time ( $1 \times 10^{-5}$  M) under visible light irradiation using (a) Ni-TiO<sub>2</sub> and (b) Cu-TiO<sub>2</sub>. It is noted that the prepared Cu-TiO<sub>2</sub> and Ni-TiO<sub>2</sub> shows more efficiency for the degradation of MB dye than the bare TiO<sub>2</sub>.

### 3.6 Photoluminescence analysis

Photoluminescence (PL) emission spectra of TiO<sub>2</sub> and Ni- and Cu- doped TiO<sub>2</sub>, as shown in Fig. 9a, b with an excitation wavelength of 320 nm. The blue-green emission bands at 468 nm and 471 nm are due to the charge transfer from Ti<sup>3+</sup> to oxygen anion in [TiO<sub>6</sub>]<sup>8-</sup> complex. This indicates the origination of bands from the intrinsic state rather than the surface state [58]. The emission edge of Ni- and Cu-doped TiO<sub>2</sub> is red shifted due to the vacancies of titanium and oxygen. The emission intensity of doped TiO<sub>2</sub> is decreased compared with TiO<sub>2</sub> which is due to the well-dispersed



**Fig. 9** PL emission spectra of **a** TiO<sub>2</sub>, and **b** Ni- and Cu-doped TiO<sub>2</sub> nanoparticles

Ni and Cu ions in anatase Titania which turns to separate noticeable. This is because of undesired Ni-Ni and Cu-Cu interactions which act as a luminescent quencher and start to severe decrease in the emission intensity [56].

### 3.7 Morphological and compositional analyses

Figure 10a-c shows FESEM images and EDS spectra of TiO<sub>2</sub>, Ni-, and Cu-doped TiO<sub>2</sub> nanoparticles. Ni- and Cu-doped TiO<sub>2</sub> nanoparticle consists agglomerates of nanosized spherical primary particles compared with TiO<sub>2</sub> nanoparticles. It is the characteristic of isotropic growth behavior of TiO<sub>2</sub>. From these results, the doping of Ni and Cu in TiO<sub>2</sub> did not alter the morphology which is attributed to the fewer amounts of Ni<sup>2+</sup> and Cu<sup>2+</sup> ions which are incorporated into the TiO<sub>2</sub> matrix. Similar type of spherical morphologies is observed by Momeni et al. [59–61]. Figure 11 shows atomic % of TiO<sub>2</sub> and doped TiO<sub>2</sub>. The EDS spectra (Fig. 11) clearly show the presence of O, Ti, Ni, and Cu. The variation in size of the dopants influences either incorporation of Ni<sup>2+</sup> and Cu<sup>2+</sup> ions into TiO<sub>2</sub> matrix during crystallization or onto the TiO<sub>2</sub> surface. These differences may be introduced from local analysis of EDS technique [56, 62, 63].

### 3.8 VSM analysis

The magnetic properties of TiO<sub>2</sub>, Ni-, and Cu-doped TiO<sub>2</sub> nanoparticles are carried out by a VSM with an applied field of 15kOe at room temperature (Fig. 12a, b) which shows ferromagnetic behavior. The room-temperature ferromagnetism (RTFM) in TiO<sub>2</sub> is due to the presence of oxygen interstitial defects [64]. Das kar et al. reported the mediated room-temperature ferromagnetism arises in host matrix which is attributed to the presence of oxygen vacancies [65–67]. In the present work, TiO<sub>2</sub> synthesized by sol-gel technique using nitric acid as chelating agent did not show magnetic behavior. The intrinsic ferromagnetic ordering is explained by theoretical model interactions such as double and superexchange, Ruderman-Kittel-Kasuya-Yosida (RKKY) and Bound Magnetic Polarons (BMP). According to BMP theory, the overlap and moment of dopant ions and vacancies of oxygen have ferromagnetic coupling between two ions via O<sub>2</sub> vacancies and this results in RTFM [68]. Figure 10 shows the ferromagnetic behavior of Ni- and Cu-doped TiO<sub>2</sub>. It is noted that, due to dopant concentration, the interaction between ions and oxygen vacancies results in either double exchange or superexchange that imparts ferromagnetism in the doped TiO<sub>2</sub> system. There is no ferromagnetic contamination which is observed both in the XRD and EDS spectra of Ni- and Cu-doped. In the present study, the weak RTFM was observed in both Ni- and Cu-doped TiO<sub>2</sub> due to the oxygen defects. Coey et al. reported the existence of RTFM in dilute magnetic oxides using BMP

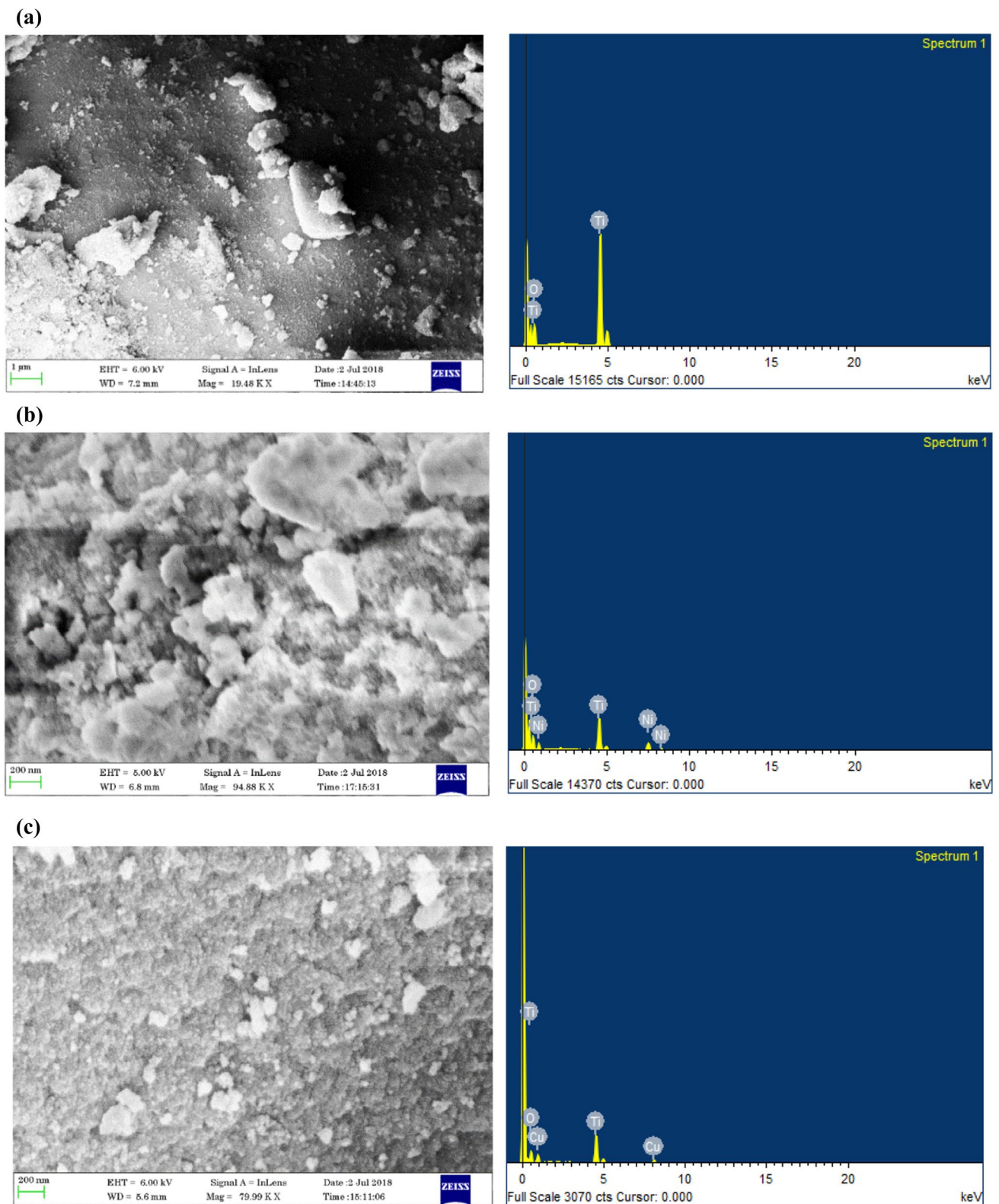


Fig. 10 FESEM images and EDS spectra of a  $\text{TiO}_2$ , b Ni-, and c Cu-doped  $\text{TiO}_2$  nanoparticles



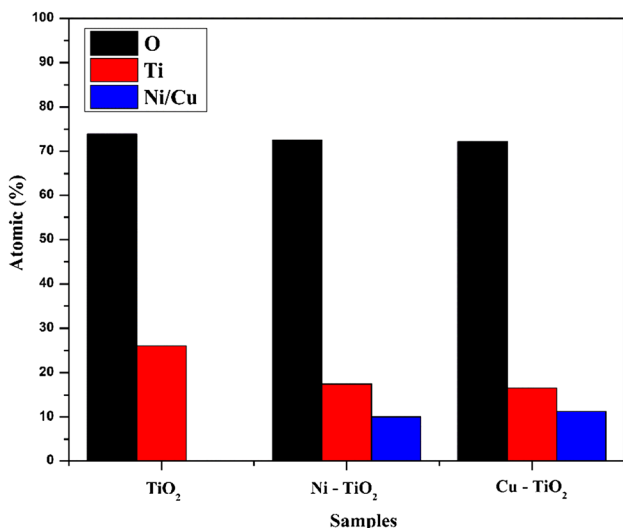


Fig. 11 Atomic (%) of TiO<sub>2</sub>, Ni-, and Cu-doped TiO<sub>2</sub> nanoparticles

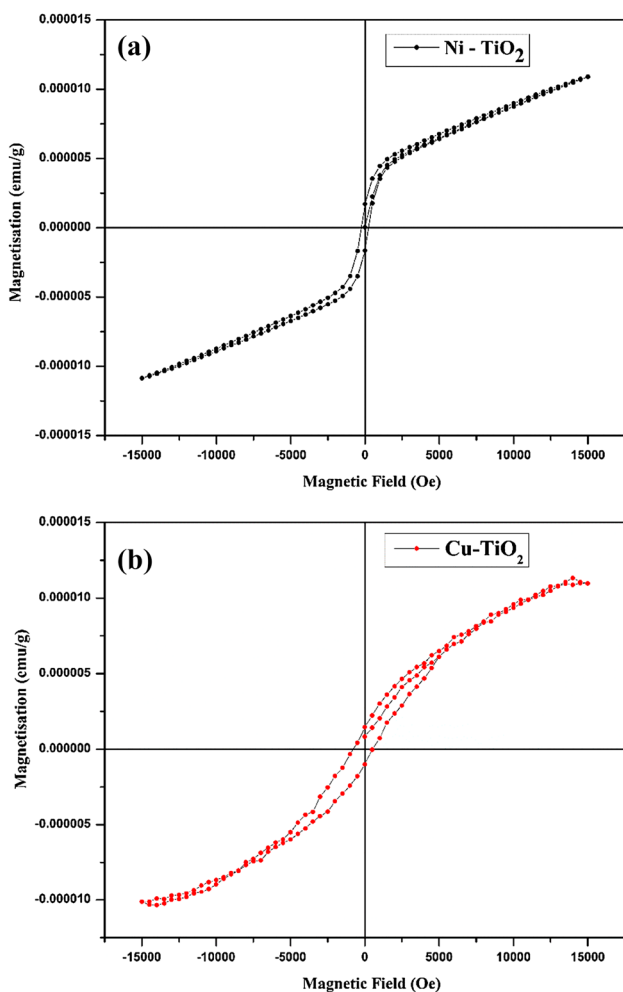


Fig. 12 VSM Plots of a Ni- and b Cu-doped TiO<sub>2</sub> nanoparticles

model [69] and Kim et al. reported that oxygen vacancies induced lattice distortion of TiO<sub>2</sub> which makes it ferromagnetic [70]. The structural analysis confirmed the replacement of Ti<sup>4+</sup> by Ni<sup>2+</sup> and Cu<sup>2+</sup> in TiO<sub>2</sub> matrix. Due to charge imbalance, O<sub>2</sub><sup>-</sup> ions escape from the lattice creating oxygen vacancies and these vacancies play an important role in trapping unpaired electrons located near to the dopant ions. In the present work, the dopant concentration (Ni and Cu—0.3 mol%) creates an ionic charge imbalance between Ni<sup>2+</sup>, Cu<sup>2+</sup> and Ti<sup>4+</sup> that produces more oxygen vacancies as also confirmed by PL spectroscopy. Thus, the probability of more BMP and their overlapping, and room-temperature ferromagnetic (RTFM) ordering is developed due to the concentration of Ni and Cu in TiO<sub>2</sub> samples. The doping of Ni<sup>2+</sup> and Cu<sup>2+</sup>, which replaces Ti<sup>4+</sup> in the samples which increase the intensity of magnetization, coercivity (H<sub>c</sub>), remanence magnetization (M<sub>r</sub>) and saturation magnetization (M<sub>s</sub>), is shown in Table 2.

It is noted that, remanence magnetization produced by Ni-TiO<sub>2</sub> is higher than that of Cu-TiO<sub>2</sub>, but its coercivity is lower than Cu-TiO<sub>2</sub> [71].

### 4 Conclusion

The structural, optical, and magnetic properties of TiO<sub>2</sub>, Ni-, and Cu-doped TiO<sub>2</sub> nanoparticles are synthesized by the sol-gel technique. XRD studies indicated the incorporation of Ni and Cu into the TiO<sub>2</sub> matrix and the crystallite size is found to be 22 nm. Micro-Raman analysis shows that anatase phase of TiO<sub>2</sub> even adding of dopants and the bands are red shifted due to the incorporation of dopants. UV-DRS measurements revealed that the band-gap decreases of doped TiO<sub>2</sub> due to the incorporation of dopants into TiO<sub>2</sub> matrix. Photoluminescence (PL) results show that an emission edge of Ni- and Cu-doped TiO<sub>2</sub> is red shifted which is attributed to the oxygen vacancies and Ti vacancies introduced after doping. The morphological analysis shows that the particles are spherical in shape with agglomeration due to the adding of dopant ions (Ni<sup>2+</sup> and Cu<sup>2+</sup>) and the EDS spectra confirm the presence of Ti, Ni, Cu, and O in the prepared samples. The photocatalytic degradation efficiency of Ni and Cu-TiO<sub>2</sub> is found to

Table 2 Magnetic parameters of Ni- and Cu-doped TiO<sub>2</sub> nanoparticles

Samples	H <sub>c</sub> (Oe)	M <sub>r</sub> (emu/g) (× 10 <sup>-5</sup> )	M <sub>s</sub> (emu/g) (× 10 <sup>-5</sup> )	M <sub>r</sub> /M <sub>s</sub>
Ni-TiO <sub>2</sub>	239.89	16.80	1.13695	0.0676
Cu-TiO <sub>2</sub>	531.76	14.18	1.08161	0.0762

be 61.04 and 68.14% which is greater than 33.32% of TiO<sub>2</sub> shows the promising future photocatalytic applications.

The doping of Ni and Cu in TiO<sub>2</sub> induces ferromagnetism and the saturation magnetization (Ms) of Ni–TiO<sub>2</sub> is higher than that of Cu–TiO<sub>2</sub>. However, the values are less shows weak ferromagnetism and it can be improved by increasing the concentration of the dopant and the synthesis process.

**Acknowledgements** The authors would like to express their gratitude to Dr. M. Karthega, Assistant Professor, Amrita Materials Science Lab, Amrita Vishwa Vidyapeetham, Coimbatore for providing their lab facilities.

## References

1. C. Klingshirm, J. Fallert, H. Zhou, J. Sartor, C. Thiele, F. Maier-Flaig, D. Schneider, H. Kalt, *Phys. Status Solidi B* **247**, 1424 (2010)
2. H. Ohno, *J. Appl. Phys.* **113**, 136509 (2013)
3. H. Ohno, *Magn. Magn. Mater.* **200**, 110 (1999)
4. T. Dietl, H. Ohno, F. Matsukura, J. Cibert, D. Ferrand, *Science* **287**, 1019 (2000)
5. D.D. Awschalom, M.E. Flatte, *Nat. Phys.* **3**, 153 (2007)
6. S. Das Sarma, *Nat. Mater.* **2**, 292 (2003)
7. S. He, H. Bai, G. Liu, Q. Li, S. Yan, Y. Chen, L. Mei, H. Liu, S. Wang, X. Han, *Appl. Phys. Lett.* **100**, 132406 (2012)
8. H. Ohno, *Nat. Mater.* **9**, 952 (2010)
9. B. Panigrahy, M. Aslam, D. Bahadur, *J. Phys. Chem. C* **114**, 11758 (2010)
10. J.M.D. Coey, S.A. Chambers, *MRS Bull.* **33**, 1053 (2008)
11. A. Ney, T. Kammermeier, K. Ollefs, S. Ye, V. Ney, T.C. Kaspar, S.A. Chambers, F. Wilhelm, A. Rogalev, *Phys. Rev. B* **81**, 054420 (2010)
12. Zirui Jia, Di Lan, Kejun Lin, Ming Qin, Kaichang Kou, Wu Guanglei, Wu Hongjing, *J. Mater. Sci. Mater. Electron.* **29**, 17122 (2018)
13. K. Olejnik, M.H.S. Owen, V. Novák, J. Mašek, A.C. Irvine, J. Wunderlich, T. Jungwirth, *Phys. Rev. B* **78**, 054403 (2008)
14. Z. Jia, K. Lin, G. Wu, H. Xing, H. Wu, *NANO Brief Rep. Rev.* **13**, 1830005 (2018)
15. L. Sang, Y. Zhao, C. Burda, *Chem. Rev.* **114**, 9283 (2014)
16. S. Qu, Y. Yu, K. Lin, P. Liu, C. Zheng, L. Wang, T. Xu, Z. Wang, H. Wu, *J. Mater. Sci. Mater. Electron.* **29**, 1232 (2018)
17. X.B. Chen, L. Liu, P.Y. Yu, S.S. Mao, *Science* **331**, 746 (2011)
18. Y.C. Nah, I. Paramasivam, P. Schmuki, *Chem. Phys. Chem.* **11**, 2698 (2010)
19. F. Bensouici, M. Bououdina, A.A. Dakhel, R. Tala-Ighil, M. Tounane, A. Iratni, T. Souier, S. Liu, W. Cai, *Appl. Surf. Sci.* **395**, 110 (2016)
20. Xuehong Li, Wu Yun, Yuhua Shen, Yan Sun, Ying Yang, Anjian Xie, *Appl. Surf. Sci.* **427**, 739 (2018)
21. Q. Wang, X. Liu, X. Wei, J. Dai, W. Li, *J. Nanomater.* **2015**, 5 (2015) (**Article ID 371582**)
22. Y. Alivov, V. Singh, Y. Ding, L.J. Cerkovnik, P. Nagpal, *Nanoscale* **4**, 10839 (2014)
23. S.A. Chambers, T. Droubay, *Appl. Phys. Lett.* **82**, 1257 (2003)
24. K.A. Griffin, A.B. Pakhomov, C.M. Wang, S.M. Heald, K.M. Krishnan, *J. Appl. Phys.* **97**, D320 (2005)
25. H.H. Nguyen, W. Prellier, J. Sakai, A. Ruyter, *J. Appl. Phys.* **95**, 7378 (2004)
26. C.M. Wang, V. Shutthanandan, S. Thevuthasan, T. Droubay, S.A. Chambers, *J. Appl. Phys.* **97**, 073502-1 (2005) (**Article ID 073502**)
27. R. Suryanarayanan, V.M. Naik, P. Kharel, P. Talagala, R. Naik, *Solid State Commun.* **133**, 439 (2005)
28. P.K. Khanna, N. Singh, S. Charan, *Mater. Lett.* **61**, 4725 (2007)
29. C.Y. Wang, C. Böttcher, D.W. Bahnemann, J.K. Dohrmann, *J. Mater. Chem.* **13**, 2322 (2003)
30. N.R.S. Farley, C.R. Staddon, L. Zhao, K.W. Edmonds, B.L. Gallagher, D.H. Gregory, *J. Mater. Chem.* **14**, 1087 (2004)
31. G. Colon, M. Maicu, M.C. Hidalgo, J.A. Navio, *Appl. Catal. B* **67**, 41 (2006)
32. K.H. Yoon, J.S. Noh, C.H. Kwon, M. Muhammed, *Mater. Chem. Phys.* **95**, 79 (2006)
33. M. Yan, F. Chen, J. Zhang, M. Anpo, *J. Phys. Chem. B* **109**, 8673 (2005)
34. M. Saleem, L. Fang, H.B. Ruan, F. Wu, Q.L. Huang, C.L. Xu, C.Y. Kong, *Int. J. Phys. Sci.* **7**, 2971 (2012)
35. A.S. Hassanien, A.A. Akl, A.H. Saaedi, *Cryst. Eng. Commun.* **20**, s1716 (2018)
36. A.A. Kl, A.S. Hassanien, *Int. J. Adv. Res.* **2**, 1 (2014)
37. A.S. Hassanien, A.A. Akl, *Phys. B* **473**, 11 (2015)
38. S. Kumar, T.K. Song, S. Gautam, K.H. Chae, S.S. Kim, K.W. Jang, *MRS Bull.* (2015). <https://doi.org/10.1016/j.materresbu.2015.02.020>
39. Wu Hongjing, Wu Guanglei, Liuding Wang, *Powder Technol.* **269**, 443 (2015)
40. H. Wu, S. Qu, K. Lin, Y. Qing, L. Wang, Y. Fan, Q. Fu, F. Zhang, *Powder Technol.* **333**, 153 (2018)
41. I. Ganesh, A.K. Gupta, P.P. Kumar, P.S.C. Sekhar, K. Radha, G. Padmanabham, G. Sundararajan, *Sci. World J.* <https://doi.org/10.1100/2012/127326>
42. M. Mikami, S. Nakamura, O. Kitao, H. Arakawa, *Phys. Rev. B* **66**, 6 (2004)
43. C. Stella, D. Prabhakar, M. Prabhu, N. Soundararajan, K. Ramachandran, *Mater. Electron.* **27**, 636 (2016)
44. J.K. Zhou, Y.X. Zhang, X.S. Zhao, A.K. Ray, *Ind. Eng. Chem. Res.* **45**, 3503 (2006)
45. Di Lan, Ming Qin, Ruisheng Yang, Shuang Chen, Wu Hongjing, Yuancheng Fan, Fu Quanhong, Fuli Zhang, *J. Colloid Interface Sci.* **533**, 481 (2018)
46. M. Sahu, P. Biswas, *Nanoscale Res. Lett.* **6**, 441 (2011)
47. J.C. Parker, R.W. Siegel, *Appl. Phys. Lett.* **57**, 943 (1990)
48. X. Xue, W. Ji, Z. Mao, H. Mao, Y. Wang, X. Wang, W. Ruan, B. Zhao, J.R. Lombardi, *J. Phys. Chem. C* **116**, 8792 (2012)
49. Biswajit Choudhury, Munmun Dey, Amarjyoti Choudhury, *Int. Nano Lett.* **3**, 25 (2013)
50. S.H. Chuang, M.L. Hsieh, S.C. Wu, H.C. Lin, T.S. Chao, T.H. Hou, *J. Am. Ceram. Soc.* **94**, 250 (2011)
51. M. Picquart, L. Escobar-alarcon, E. Torres, T. Lopez, E. Haro-Poniatowski, *J. Mater. Sci.* **37**, 3241 (2002)
52. Joseph B. Lambert et al., *Introduction to Organic Spectroscopy* (Macmillan Publisher, New York, 1987)
53. Y. Nagao, A. Yoshikawa, K. Koumot, T. Kato, Y. Ikuhara, H. Ohta, *Appl. Phys. Lett.* **97**, 172112 (2010)
54. J.C.S. Wu, C.H. Chen, *J. Photochem. Photobiol. A* **163**, 509 (2004)
55. T. Morikawa, R. Asahi, T. Ohwaki, K. Aoki, Y. Taga, *J. Appl. Phys.* **40**, L561 (2001)
56. M. Pal, U. Pal, J.M.G.Y. Jilmenez, F. Perez-Rodriguez, *Nanoscale Res. Lett.* **7**, 1 (2012)
57. K.R. Anju, T. Radika, R.J. Ramaligham, H.A. Al-Loheda, *Optik* **165**, 408 (2018)
58. A.K. Tripathi, M.C. Mathpal, P. Kumar, V. Agrahar, M.K. Singh, S.K. Mishra, M.M. Ahmad, A. Agarwal, *Adv. Matt. Lett.* **6**, 201 (2015)

59. M.M. Momeni, Y. Ghayeb, F. Ezati, J. Colloid Interface Sci. **514**, 70 (2018)
60. S. Challagulla, K. Tarafder, R. Ganesan, S. Roy, J. Phys. Chem. C **121**, 27406 (2017)
61. J. Zhao, Y. Yang, Y. Li, L. Zhao, H. Wang, G. Song, G. Tang, Sol. Energy Mater. Sol. Cells **168**, 62 (2017)
62. I. Ganesh, A.K. Gupta, P.P. Kumar, P.S.C. Sekhar, K. Radha, G. Padamanathan, G. Sundarajan, Sci. World J. (2012). <https://doi.org/10.1100/2012/127326>
63. B. Unlu, S. Cakar, M. Ozacar, Sol. Energy **166**, 441 (2018)
64. H. Gao, J. Tian, H. Zheng, F. Tan, W. Zhang, J. Sol Gel Sci. Technol. **74**, 521 (2015)
65. A.K. Das, M. Kar, A. Srinivasan, Phys. B **448**, 112 (2014)
66. B. Parveen, M.U. Hassan, Z. Khalid, S. Riaz, S. Naseem, J. Appl. Res. Technol. (2017). <https://doi.org/10.1016/j.jart.2017.01.009>
67. H. Wu, G. Wu, Y. Ren, L. Yang, L. Wang, X. Li, J. Mater. Chem. C **3**, 7677 (2015)
68. M.J. Calderon, S. Das Sarma, Ann. Phys. **332**, 2618 (2007)
69. M.D. Coey, M. Venkatesan, C.B. Fitzgerald, Nat. Mater. **4**, 173 (2005)
70. D. Kim, J. Hong, Y.R. Park, K.J. Kim, J. Phys. Condens. Matter **21**, 195405 (2009)
71. B. Praveen, M.U. Hassan, Z. Khalid, S. Riaz, S. Naseem, J. Appl. Res. Technol. **15**, 132 (2017)

**Publisher's Note** Springer Nature remains neutral with regard to jurisdictional claims in published maps and institutional affiliations.